The Three-Dimensionalization of Stratified Flow over Two-Dimensional Topography

Ya. D. Afanasyev and W. R. Peltier

Department of Physics, University of Toronto, Toronto, Ontario, Canada

(Manuscript received 22 November 1996, in final form 15 April 1997)

ABSTRACT

The authors present a series of new analyses of the problem of stratified flow over a localized two-dimensional obstacle, focusing upon the detailed dynamical characteristics of the flows that develop when the Froude number is such that the forced internal waves "break" above their topographic source. Results demonstrate that when the flow is restricted to evolve in two space dimensions, then the intensity of the Kelvin–Helmholtz-like (K–H) perturbations that form in the downstream shear layer that separates the accelerated low-level jet in the lee of the obstacle and the overlying region of decelerated flow increases dramatically with the governing parameter NU/g (U and N are, respectively, the velocity and buoyancy frequency characteristic of the upstream incident flow, while g is the gravitational acceleration). This nondimensional parameter represents the ratio of the acceleration that a fluid particle feels in the wave to the gravitational acceleration and measures the importance of non-Boussinesq effects. A marked change in the global characteristics of the flow is shown to occur with increasing NU/g, characteristics that include the speed of downstream propagation of the so-called chinook front, the drag exerted by the flow on the obstacle, and the intensity of the K–H instability induced pulsations of the surface velocity field. When the flow is allowed to access the third spatial dimension, the authors demonstrate that it develops intense three-dimensional motions in the regions where overturning of the isentropes in the otherwise stably stratified fluid takes place. An instability of convective type first appears in the form of streamwise-oriented vortices of alternating sign. This instability erodes the downstream propagating K–H billows, eventually leading to the complete arrest of their continued propagation as they "dissolve" into fully developed turbulent flow.

1. Introduction

It is important to study hydrodynamic flows of geophysical origin not only because of their many practical connections to the understanding of atmospheric and oceanographic phenomena, but also because such flows often reveal the influence of fundamental hydrodynamic interactions that may be extremely difficult to adequately investigate in the laboratory. An especially interesting example of such flows is certainly provided by the severe downslope windstorms that are observed in the lee of major mountain ranges such as the foehn of Switzerland, the bora of Yugoslavia, and the chinook of North America. These flows have a long history of serious investigation that has been reflected in the meteorological literature for at least 50 years. It is now rather clear that the specific dynamical processes that underly the occurence of this phenomenon include, primarily, the "breaking" of upward-propagating internal waves that are forced orographically and a late stage Kelvin–Helmholtz instability of the low-level jet that appears in the lee of the obstacle in consequence of the wave–mean flow interaction induced by this primary wave-breaking event.

The first step in this sequence of events is now well understood and is connected with the fact that, when a density stratified fluid flows over an obstacle, a field of internal waves is launched that propagates in the vertical. If the incident flow has uniform velocity profile (U) and constant buoyancy frequency (N), then such waves propagate vertically without impediment so long as their amplitude remains small. Normally, however, it is inevitable that the wave amplitude grows with height in consequence of the decreasing density of their environment and therefore that the waves eventually "break" by inverting the local density stratification. As a result of such wave breaking, downward-propagating waves are induced due to nonlinear scattering and/or reflection at the wave-induced critical level (Peltier and Clark 1979, 1983; Bacmeister and Schoeberl 1989). When the obstacle that forces the waves is sufficiently high relative to the natural internal vertical scale of the flow U/N, then wave breaking may occur at a low level within one wavelength from the surface. Both on the basis of numerical analyses (Peltier and Clark 1979, 1983; Durran 1986; Scinocca and Peltier 1989; Laprise and Peltier 1989a) and laboratory experiments (Rottman and Smith 1989) it is now well understood that such low-level wave breaking results in a resonant amplifi-

Corresponding author address: W. R. Peltier, Department of Physics, University of Toronto, Toronto, ON M5S 1A7, Canada.
E-mail: peltier@chinook.physics.utoronto.ca

cation of the low-level flow due to the constructive interference between the upgoing and downgoing waves. This in turn leads to a dramatic acceleration of the flow in the lee of the obstacle and an equally dramatic increase in the drag exerted by the flow on the obstacle. In its fully developed form, at an instant of time sufficiently long after the onset of breaking, the flow closely resembles a hydraulic jump of the kind that may be generated by the flow of constant density fluid with a free surface over an isolated obstacle (Long 1953). A simple model, based on Long's (1953) analysis for the steady flow of a uniformly stratified fluid over an obstacle, has been suggested by Smith (1985) in which the elevated region of mixed fluid maintained by wave breaking is assumed to represent an internal ''block'' around which streamlines are split, and this simple model has been shown to mimic several of the properties of the time-averaged high-drag state, though it fails to account for the intense time dependence that is actually characteristic of this state (Peltier 1993).

The most recent numerical simulations (Scinocca and Peltier 1989; Peltier and Scinocca 1990) of this phenomenon demonstrate that a typical feature of the flow is the eventual emergence of Kelvin–Helmholtz instability in a shear layer that develops between the low-level high velocity jet and the overlying almost stagnant region created by wave breaking. It appears that this instability, once it occurs, thereafter plays a fundamental role in controlling the global dynamics of the flow (Peltier and Scinocca 1990). In most previous numerical simulations of the downslope windstorm phenomenon, this initial sequence of events has been described using two-dimensional models. Several three-dimensional calculations of downslope windstorms as well as other relevant studies of internal gravity waves in atmospheric and oceanic applications (Peltier and Clark 1983; Clark and Farley 1984; Klaassen and Peltier 1985a,b,c; Winters and Riley 1992; Clark et al. 1994) have demonstrated that three-dimensional effects and instability structures are important in these flows. For example, numerical simulations of breaking gravity waves (e.g., Andreassen et al. 1994) reveal vigorous instability structures and in particular the development of streamwise vortices of alternating sign that induce a more rapid breakdown of the unstable wave relative to the two-dimensional case. The appearance of streamwise vortices is also a typical feature of secondary instability of unstable stratified free shear layers. It is well known that these layers are susceptible to a primary instability of the Kelvin–Helmholtz type. High-density fluid is pulled above low-density fluid in the rollup of the primary spanwise Kelvin–Helmholtz billows. This causes the development of a secondary mode of instability that is of convective type (Klaassen and Peltier 1985a,b,c). Numerical simulations (e.g., Caulfield and Peltier 1994) and laboratory experiments (Thorpe 1985, 1987; Schowalter et al. 1994) all demonstrate that it is precisely the Klaassen–Peltier (K–P) instability that drives the growth of streamwise longitudinal rolls of alternate signed vorticity and it is these motions that subsequently lead to the complete turbulent collapse of the billow core. The K–P instability is also responsible for the growth of the streamwise vortex streaks in the internal wave-breaking simulations of Andreassen et al. (1994).

Most previous two-dimensional simulations of the severe downslope windstorm phenomenon have focused on the analysis of effects due to the nonlinearity of the finite-amplitude lower boundary condition and on the influence of nonhydrostaticity. In the present study, attention will rather be focused on the importance of non-Boussinesq effects. The numerical experiments described in this paper demonstrate that the secondary Kelvin–Helmholtz instability, and hence all global characteristics of the flow, are extremely sensitive to variations of the nondimensional parameter that measures the importance of non-Boussinesq effects. Since previous three-dimensional calculations of flow evolution contained insufficient spatial resolution to resolve finescale three-dimensional instability structures we will also present herein a single high-resolution simulation of the flow in three dimensions. As we will show, the initial structure of the three-dimensional motions that develop are fully explicable in terms of the above-mentioned K–P instability, which will be seen to induce the appearance of streamwise vortex streaks. Our analyses will therefore further extend the range of circumstances in which this instability is shown to control the onset of three-dimensional motions in stratified flows.

In the following sections of this paper, the equations of motion and boundary conditions employed in the numerical model that we employ are discussed in section 2, while section 3 contains an analysis of the main governing parameters of the flow. A number of simple theoretical considerations concerning the dynamics of a wave field launched by localized topography are offered in section 4. The new sequence of simulations that document the importance of non-Boussinesq effects on the severe downslope windstorm transition in two dimensions are described and discussed in section 5, while the results from our high-resolution representative three-dimensional simulation are presented in section 6. Conclusions are summarized in section 7.

2. Model equations and boundary conditions

The numerical model to be employed to perform the simulations discussed herein is essentially that described in Clark (1977) and first employed in the context of analyses of topographically forced internal waves in Clark and Peltier (1977). The model is based upon the anelastic approximation to the equations of motion (e.g., Batchelor 1967), which may be written in the form

$$\overline{\rho}\frac{du_i}{dt} = -\partial_i p' - \delta_{i3}g\rho' + \partial_j\overline{\rho}K_M D_{ij} \qquad (1)$$

$$\partial_i(\overline{\rho}\,u_i) = 0 \qquad (2)$$

$$\overline{\rho}\frac{d\theta}{dt} = \partial_i(\overline{\rho}\,K_H\partial_i\theta), \qquad (3)$$

in which u_i ($i = 1, 2, 3$) are the components of velocity in (x, y, z) Cartesian coordinates, θ is potential temperature, and K_M and K_H are mixing coefficients for momentum and heat. Here, p' and ρ' are pressure and density fluctuations, respectively, such that

$$p = \overline{p}(z) + p'(x, y, z, t) \qquad (4)$$

$$\rho = \overline{\rho}(z) + \rho'(x, y, z, t) \qquad (5)$$

$$\frac{d\overline{p}}{dz} = -\overline{\rho}\,g. \qquad (6)$$

The overbar denotes a hydrostatic background state variable, and the deformation tensor D_{ij} is given by

$$D_{ij} = \partial_j u_i + \partial_i u_j - \frac{2}{3}\delta_{ij}\partial_k u_k. \qquad (7)$$

Similar to the set of equations one obtains in the Boussinesq approximation, the above set ignores variations of density away from the height dependent background field $\overline{\rho}(z)$ except where such variations are multiplied by the gravitational acceleration g. Because the density variations are defined as deviations from the background density $\overline{\rho}(z)$, rather than from a constant, these equations incorporate an important non-Boussinesq effect. The connection between the thermodynamic variables p, ρ, θ will be herein assumed to be given by the ideal gas equation of state, namely

$$p = \rho RT. \qquad (8)$$

Our anelastic equations are formulated in terms of potential temperature θ rather than absolute temperature T, the two variables being related by the definition

$$\theta = T\left(\frac{p}{p_0}\right)^{-\kappa}, \qquad (9)$$

in which p_0 is the surface pressure at $z = 0$, and $\kappa = R/C_p = 0.286$ for dry air.

A linearization of (8) and (9) results in

$$\rho' = \frac{p'}{\gamma RT} - \overline{\rho}\frac{\theta'}{\overline{\theta}}, \qquad (10)$$

in which $\gamma = C_p/C_v$ is the usual ratio of specific heats. To parameterize turbulent eddy mixing on the subgrid scale, the eddy mixing coefficient for momentum K_M is assumed to be representable by the first-order closure

$$K_M = \begin{cases} (c\Delta)^2|\text{def}|(1 - \text{Ri})^{1/2}, & \text{if Ri} \leq 1; \\ 0, & \text{otherwise.} \end{cases} \qquad (11)$$

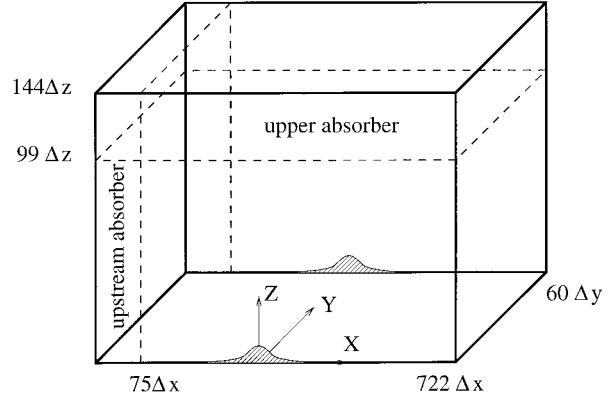In (11), c is a numerical constant, Δ is a measure of the

FIG. 1. The model domain.

grid resolution [for the two-dimensional case $\Delta = (\Delta x\Delta z)^{1/2}$ and for the three-dimensional case $\Delta = (\Delta x\Delta z\Delta y)^{1/3}$], and Ri is the local gradient Richardson number

$$\text{Ri} = g\frac{d\,\ln\theta}{dz}(\text{def})^{-2}, \qquad (12)$$

in which the total deformation def is defined as

$$(\text{def})^2 = \frac{1}{2}\sum_i\sum_j D_{ij}^2. \qquad (13)$$

This first-order closure for the turbulent diffusion enhances viscous dissipation where the motion becomes sufficiently complicated that the scale of the grid can no longer resolve it. The eddy mixing coefficient for heat, K_H, is taken to be equal to K_M so that the eddy Prandtl number Pr $= K_M/K_H$ is unity.

In Fig. 1 we present a schematic of the model domain to be employed for the purpose of the three-dimensional calculations to be discussed in what follows. For the initial two-dimensional integrations the XZ section of the domain is employed. At the inflow and outflow boundaries open boundary conditions are applied, while a rigid lid condition is imposed on the upper horizontal boundary of the model. In order to simulate an unbounded fluid, an absorbing region (with enhanced friction) is employed in the top third of the model domain. This is introduced to prevent the reflection of internal waves that are incident upon the upper boundary from below. A similar absorbing region is installed upstream adjacent to the inflow boundary to eliminate the influence of upstream-propagating perturbations on the inflow fields.

The topography (h_s) used in all the simulations is two-dimensional and of the simple symmetric "bell shaped" form

$$h_s(x) = \frac{h}{1 + \left(\dfrac{x}{a}\right)^2}, \qquad (14)$$

in which h is the obstacle height and a its half-width. The parameters h and a are varied between different experiments, but their ratio, $h/a = 0.1$, will be kept constant in order to ensure that the dominant response to the topographic forcing consists of predominantly hydrostatic waves.

In most of the experiments to be discussed in the present paper, the upstream profiles of u and θ will be assumed to be given by

$$\bar{u} = U = \text{const} \tag{15}$$

$$\bar{\theta} = \theta_0 \exp\left(\frac{zN^2}{g}\right), \tag{16}$$

from which bouyancy frequency N may be determined as

$$N^2 = \frac{g}{\bar{\theta}} \frac{d\bar{\theta}}{dz}, \tag{17}$$

and $N = \text{constant} = 0.01 \text{ s}^{-1}$ will be fixed in the sequence of experiments that we intend to describe. The background density in the anelastic basic state then has the simple analytic form

$$\bar{\rho}(z) = \rho_0 \exp\left(-\frac{z}{H}\right), \tag{18}$$

in which the density-scale height H is related to the buoyancy frequency through the relationship

$$H = \kappa \frac{g}{N^2} \approx 28.6 \text{ km}. \tag{19}$$

The three-dimensional calculations are initialized from the two-dimensional calculations. For the purpose of these analyses, the flow is allowed to develop in three dimensions only after some period of two-dimensional evolution. This was done to avoid the introduction of possibly spurious three-dimensional effects due to the starting transient and also to conserve computational resources, since the three-dimensional calculations are extremely expensive both in terms of computer execution time and memory. The analyses that we will report herein have all been performed on the CRAY J916 computer system in our laboratory in Toronto, Ontario.

3. Governing parameters

Dimensional analysis requires that a vertically unbounded flow with constant U and N above an obstacle that is characterized by the two length scales h and a be governed by these five nondimensional parameters:

$$(F_v, F_h, F_\rho, \text{Re}, \text{Pr}). \tag{20}$$

The first three members of this set are all appropriately defined Froude numbers, namely

$$F_v = \frac{hN}{U}, \qquad F_h = \frac{aN}{U}, \qquad F_\rho = \frac{HN}{U}.$$

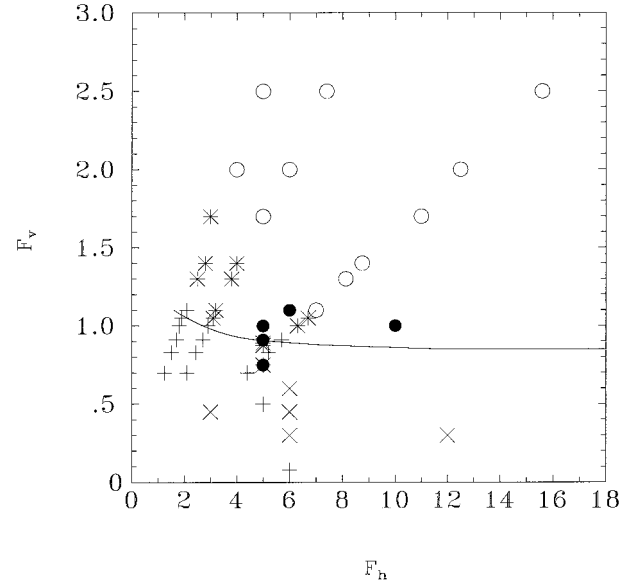Previous analyses of the flows to be investigated herein

FIG. 2. Regime diagram in space of parameters F_v and F_h: open circles ($\bigcirc$) show wave breaking at low level and formation of the modified flow (laboratory experiments by Rottman and Smith 1989); filled circles ($\bullet$) show formation of the modified flow, high drag regime [numerical experiments by Bacmeister and Schoeberl (1989) and by Scinocca and Peltier (1989)]; asterisks (*) show intermittent wave breaking at low level (laboratory experiments by Rottman and Smith 1989); crosses (+) show no wave breaking at low level [laboratory experiments by Rottman and Smith (1989), numerical simulations by Bacmeister and Schoeberl (1989) and by Scinocca and Peltier (1989)]; and exes ($\times$) show breaking at high levels, intermittent high drag (numerical experiments by Bacmeister and Schoeberl 1989). The solid curve represents a condition for critical steepening of the streamlines obtained by Laprise and Peltier (1989b).

have been focused almost entirely upon the parameters F_v and F_h. In Fig. 2, we summarize the results of several such previous analyses by indicating qualitatively, in the F_v–F_h plane, the characteristics of the statistical equilibrium states obtained in the simulations. The above three Froude numbers represent the ratios of different length scales (namely, obstacle height h, obstacle half-width a, and density-scale height H) to the intrinsic vertical length scale of the flow U/N. The latter length scale is clearly the height to which a fluid particle may ascend moving vertically with initial velocity U from its equilibrium density level in the stratified fluid with buoyancy frequency N (it is clear, for example, that when $F_v > 1$, upstream blocking must occur). The length scale U/N is also the inverse vertical wavenumber $k_G^{-1} = \lambda_z/2\pi = U/N$ of stationary hydrostatic internal waves. The Froude number F_v is a measure of the degree of nonlinearity (due to the finite amplitude lower boundary condition) to be expected of the flow. An important phenomenon, whose occurence is governed by F_v, is the breaking of upward-propagating internal waves. Breaking occurs when a streamline at some height locally excedes a vertical orientation, so that the flow in this vicinity becomes locally unstable against convection. Wave breaking occurs at displacement maxima in

the (hydrostatic) wave field that are separated vertically by a wavelength. When F_v is small, breaking begins far from the surface due to the influence of the upward decrease of density in the anelastic basic state and then descends from one displacement maximum to the one below (e.g., Bacmeister and Schoeberl 1989). In contrast, when $F_v \gtrsim F_v^c$ (where F_v^c is some critical value of F_v), breaking appears at the lowest displacement maximum at $z_c \approx (3/4)\lambda_z = (3\pi/2)(U/N)$ (the precise height of the lowest maximum for the non-Boussinesq flow will be considered further in this paper and will be shown to be of fundamental importance) and then at the subsequent levels above (Peltier and Clark 1979). In the latter case the flow is fundamentally different from that for subcritical conditions. A bifurcation occurs that results in a resonant amplification of the low-level flow in the lee of the obstacle. Linear wave theory (in the hydrostatic limit) gives the critical value for the Froude number at the bifurcation point to be $F_v^c = 1$, while the finite-amplitude solution (Miles and Huppert 1969) of the steady-state equations originally derived by Long (1953) gives the value $F_v^c = 0.85$ when the bell-shaped topography (14) is assumed to force the internal waves. The solid curve in Fig. 2 shows the condition of critical steepening of the streamlines that has been obtained by solving Long's model numerically (Laprise and Peltier 1989b). Full transient numerical simulations by Scinocca and Peltier (1989) of the unsteady nonlinear problem have delivered a similar value $F_v^c \approx 0.9$.

The second Froude number $F_h = aN/U$ in the list (20) provides a measure of the importance of nonhydrostatic effects. Since the horizontal and vertical wavenumbers of the steady wave field launched by the obstacle are related by

$$\frac{k_z^2 U^2}{N^2} = 1 - \frac{k_x^2 U^2}{N^2} \qquad (21)$$

and the dominant horizontal length scale of the wave field is determined by the obstacle width $k_x \sim a^{-1}$, it is clear that when F_h is large ($k_x U/N \to 0$) the wave field consists of freely propagating waves with $k_z \approx k_G = N/U$. In contrast, when F_h is small, the right-hand side of (21) becomes negative, which means that the disturbance is trapped in the vertical and evanescent [the so-called potential flow regime; see, e.g., Gill (1982)]. Note that when $F_h \sim 1$ the scale of the forcing (mountain halfwidth) matches the wavelength of the wave field (Peltier and Clark 1979) and, as a result, a steady pattern of nonhydrostatic "lee waves" is established behind the obstacle.

The third Froude number, $F_\rho = HN/U \propto g/NU$, is the ratio of the gravitational acceleration to the acceleration of a fluid particle in the wave and measures the importance of non-Boussinesq effects. Previous numerical simulations (Bacmeister and Schoeberl 1989) of the flow for subcritical F_v show that, for smaller F_ρ, the typical time of flow evolution decreases, while the scales

of upward- and downward-propagating waves appear to be independent of F_ρ. The dependence of major flow characteristics on F_ρ for $F_v > F_v^c$ will be the main focus of the analyses to be presented in the work to be reported herein and this has not been previously discussed.

It appears that flow characteristics in the supercritical regime also significantly depend upon the Reynolds number of the flow, which we may define as

$$\text{Re} = \frac{Uk_G^{-1}}{K_M} = \frac{U^2}{NK_M}. \qquad (22)$$

Using (11) and scaling deformation as $\text{def} \sim U/k_G^{-1} = N$, it is clear that in the regions of the flow where $\text{Ri} < 1$, the Reynolds number can be estimated as

$$\text{Re} \approx \frac{U^2}{N^2 c^2 \Delta x \Delta z}. \qquad (23)$$

The last parameter in the set (20) is the Prandtl number $\text{Pr} = K_M/K_H$, which is the ratio of diffusivities of momentum and heat. As mentioned previously, in all of the analyses that follow, this will be taken to be equal to unity.

4. The height of the critical steepening level

Following Peltier and Clark (1979), consider the linear solution for the free stream deflection $\zeta(x, z)$ in the hydrostatic limit, which has the functional form

$$\zeta(x, z) = \frac{a^2 h}{x^2 + a^2} \exp\left(\frac{z}{2H}\right) \cos k_G z$$

$$- \frac{ahx}{x^2 + a^2} \exp\left(\frac{z}{2H}\right) \sin k_G z. \qquad (24)$$

The condition for instability of the wave is $\partial \zeta/\partial z > 1$. In the limit $H \gg z$, it is found that the first steepening level occurs where $k_G z_c = 3\pi/2$ and $x = 0$. To next highest order, one may construct a solution of

$$\frac{\partial \zeta}{\partial z}(x, z) - 1 = 0 \qquad (25)$$

in the form

$$k_G z_c = \frac{3\pi}{2} - \epsilon^{1/2} k_G z_1, \qquad x = 0, \qquad (26)$$

where $\epsilon = (2k_G H)^{-1} = (2F_\rho)^{-1}$ is a small parameter and $k_G z_1$ is of order of unity. Substitution of (26) into (25) immediately gives

$$k_G z_c = \frac{3\pi}{2} - \left(\frac{3\pi}{2F_\rho}\right)^{1/2}. \qquad (27)$$

The graph of (27) is shown in Fig. 3a. It is therefore clear that for smaller F_ρ the level of wave breaking, to which we may refer as a wave-induced critical level, descends. Numerical solution of (25) also shows that
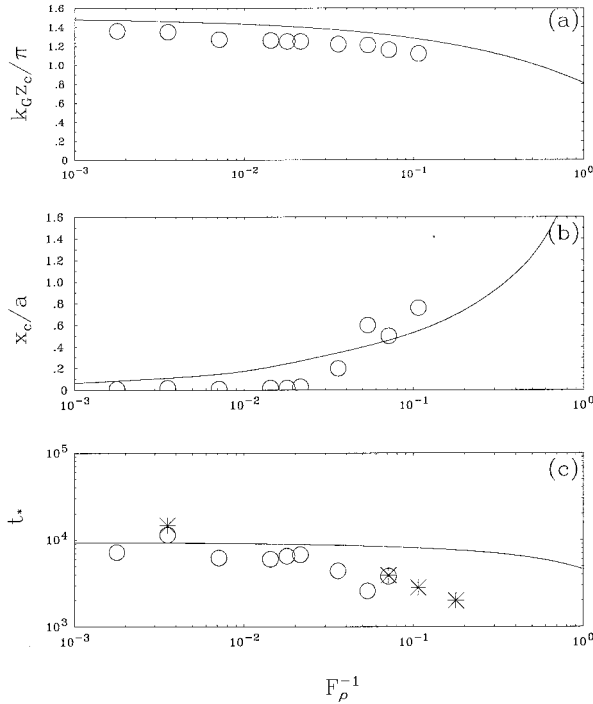
FIG. 3. Characteristics of wave breaking for different values of $(F_\rho)^{-1}$: (a) normalized height of breaking level. The solid curve represents the dependence (27). (b) Nondimensional downstream shift of the wave breaking region. The solid curve represents the numerical solution of (25). (c) Virtual origin of the modified flow regime. The solid curve represents the estimate of two-way delay obtained from (27) and (32). Asterisks denote the experiments with the relatively high Reynolds number.

the point at which critical steepness is achieved shifts downstream as F_ρ decreases (Fig. 3b).

To estimate a typical time that would be required for a wave packet to reach the critical level and for a reflected wave to return to the "ground" (two-way group delay), one needs the vertical component of the group

velocity. This may be estimated on the basis of the following conventional wave equation for linear disturbances in a stratified fluid:

$$\frac{\partial^2}{\partial t^2}\left(w_{xx} + w_{zz} + \frac{1}{H}w_z\right) + N^2 w_{xx} = 0, \quad (28)$$

in which w is the vertical velocity perturbation. For disturbances of the form

$$w \sim \exp[i(k_x x + k_z z - \omega t)], \quad (29)$$

the dispersion relation is simply, as is well known,

$$\omega^2 = \frac{N^2 k_x^2}{k_x^2 + k_z^2 - \dfrac{1}{4H^2}}. \quad (30)$$

From (30) one may obtain the vertical component of the group velocity as

$$c_{gz} = \frac{\partial \omega}{\partial k_z} = \frac{-\omega k_z}{k_x^2 + k_z^2 - \dfrac{1}{4H^2}}. \quad (31)$$

Since the steady disturbance launched by the obstacle has $\omega = k_x U$, we have

$$\frac{c_{gz}}{U} = \frac{k_x U}{N}\left[1 - \left(\frac{k_x U}{N}\right)^2 + \left(\frac{1}{2F_\rho}\right)^2\right]^{1/2}. \quad (32)$$

From (32) and (26) one can estimate the two-way group delay using the appropriate value of the dominant horizontal length scale k_x^{-1} of the waves, which is determined by the horizontal scale of the obstacle, a. The estimate for $k_x \approx a^{-1}$ (the value employed in the numerical simulations of Bacmeister and Schoeberl 1989), is shown in Fig. 3c.

TABLE 1. Parameters used in numerical experiments.

| Experiment	U (m s^{-1})	Δx (m)	Δz (m)	c	$F\rho$	F_ρ^{-1}	Re
1	0.5	20	10	0.23	560	0.0018	240
2	1.0	50	25	0.23	280	0.0036	150
3	1.0	30	10	0.23	280	0.0036	550
4	1.0	50	25	0.115	280	0.0036	600
5	1.0	40	20	0.10	280	0.0036	1200
6	1.0	40	20	0.01	280	0.0036	1.2×10^5
7	2.0	100	50	0.23	140	0.0071	150
8	4.0	200	100	0.23	70	0.014	150
9	5.0	250	125	0.23	57	0.017	150
10	6.0	300	150	0.23	47	0.021	150
11	10.0	500	250	0.23	28	0.036	150
12	15.0	400	250	0.23	19	0.053	420
13	20.0	400	250	1.15	14	0.071	30
14	20.0	400	250	0.69	14	0.071	84
15	20.0	400	250	0.23	14	0.071	760
16	30.0	300	200	0.23	9.3	0.11	2800
17	50.0	200	150	0.92	5.6	0.18	990
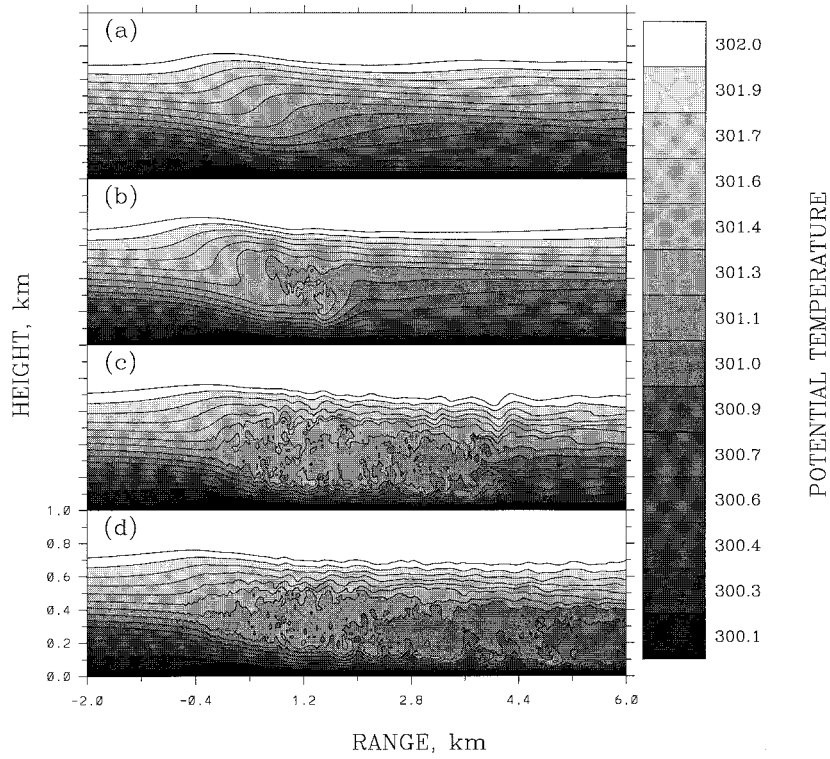
FIG. 4. Contour plots of potential temperature for two simulations (lines 6, 14 in Table 1):
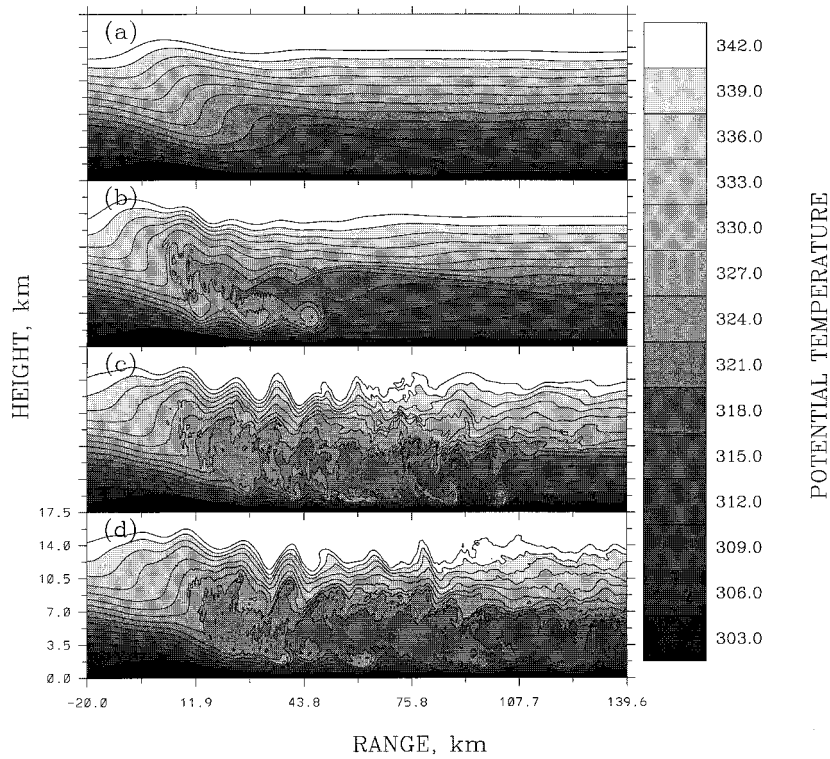$U = 1.0$ m s^{-1}, $t = 120$ (a), 240 (b), 360 (c), 480 min (d).

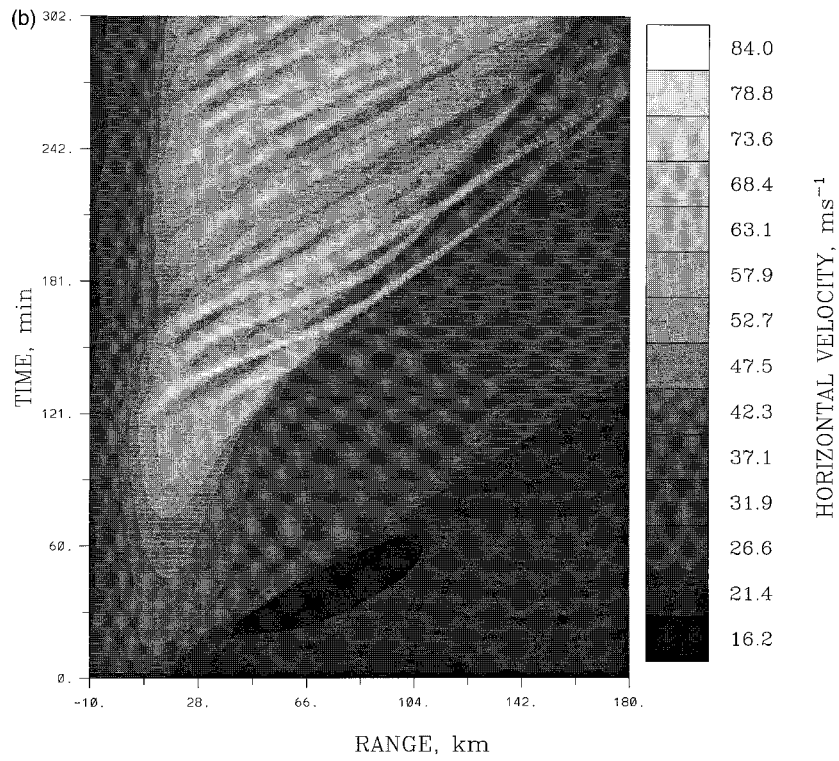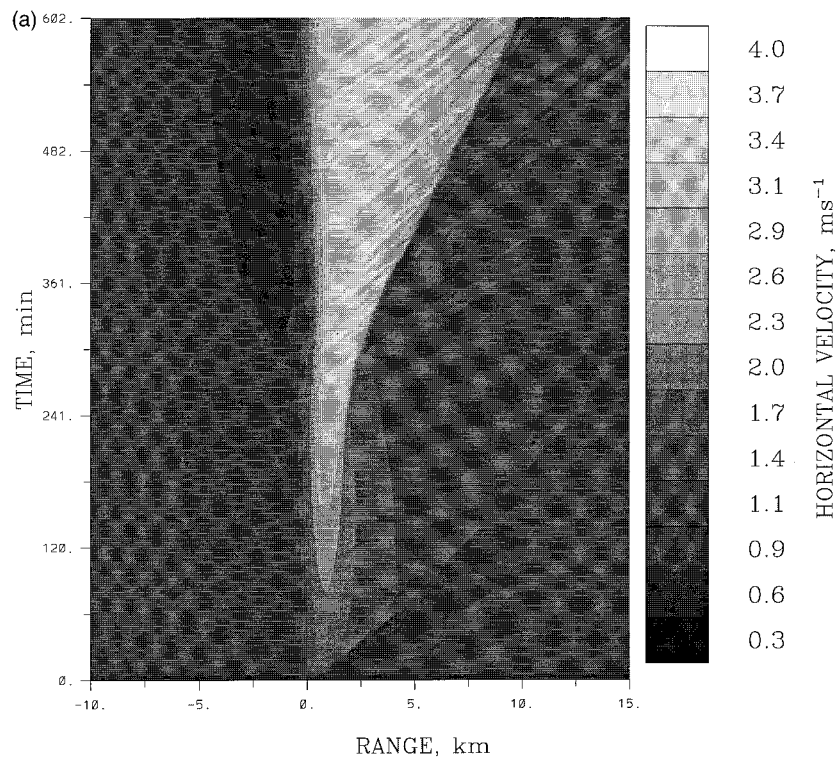FIG. 5. As in Fig. 4 but $U = 20$ m s^{-1}, t = 60 (a), 120 (b), 180 (c), 240 min (d).

Fig. 6. Hovmöller plot of surface horizontal velocity for three simulations (lines 2,14,16 in Table 1): (a) $U = 1.0$ m s^{-1}, (b) $U = 20$ m s^{-1}, (c) $U = 50$ m s^{-1}.
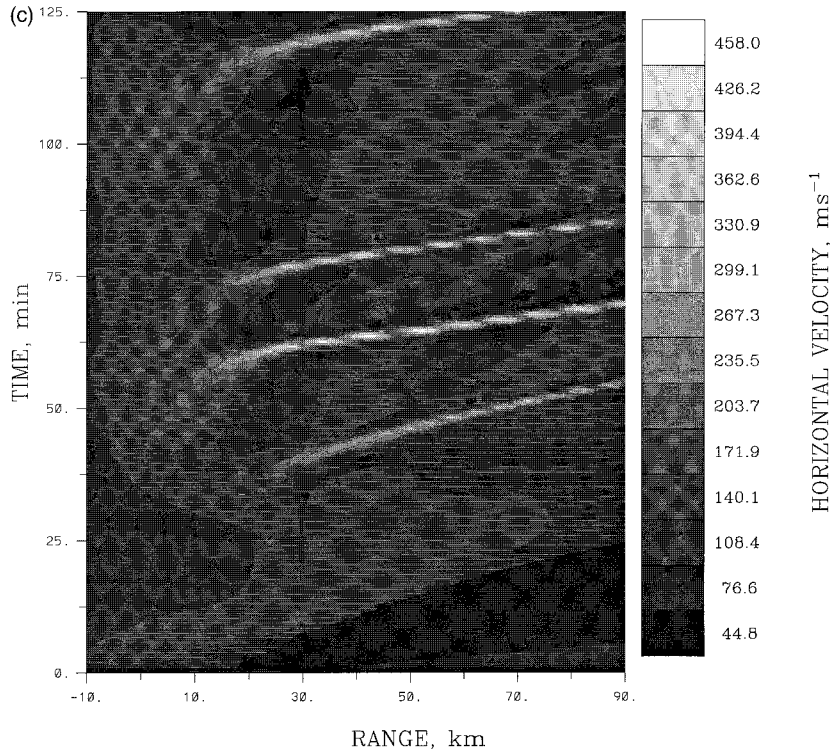
FIG. 6. (*Continued*)

5. Results and interpretation of the two-dimensional simulations

The dimensional parameters *h, a, N,* and *U* in our numerical experiments are chosen so that the nondimensional Froude numbers are $F_v = 1$ and $F_h = 10$. The parameter F_ρ may then be varied by changing the inflow velocity *U*. The eddy diffusion coefficient *c* in (11), as well as grid scales $\Delta x, \Delta z,$ are varied and thus the Reynolds number also changes from experiment to experiment.

Several numerical solutions of the initial value prob-
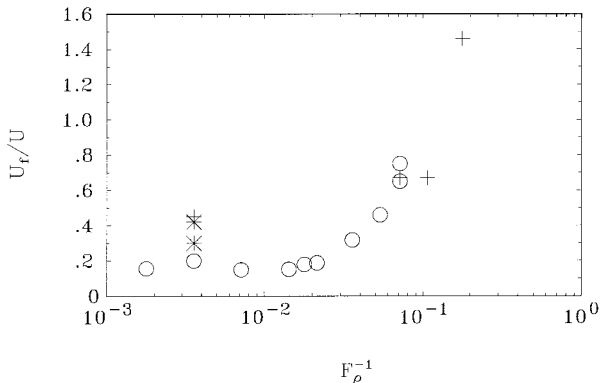
FIG. 7. Nondimensional speed of the modified flow front (chinook front) propagation for different values of $(F_\rho)^{-1}$. Different symbols indicate different Re values: (○) Re < 420, (*) 420 < Re < 550, (+) Re > 750.

lem have been constructed for different values of F_ρ and Re (Table 1). In all experiments, a typical picture of formation and subsequent evolution of the basic flow structure (accelerated low-level jet and decelerated overlying mixed layer) was observed (Figs. 4, 5). The downstream region of modified flow has a well-defined sharp front (the so-called chinook front) that propagates downstream with almost constant speed (Fig. 6). The chinook front propagation speed is obviously an important global property of the flow and it is a characteristic that can be measured easily as the slope of the line separating regions of high and low velocity in a sequence of typical Hovmöller diagrams (Fig. 6) that presents the temporal variation of the horizontal velocity field across the entire lower boundary of the domain of the evolving flow. Results for the velocity of chinook front propagation deduced from such data are shown in Fig. 7. On the basis of these tests, it is clear that, as F_ρ^{-1} increases (*U* increases, and thus non-Boussinesq effects become more important), the ratio of chinook front speed (U_f) to the inflow velocity (*U*) rises from an almost constant value at low F_ρ^{-1} to a very high value at high F_ρ^{-1}.

A further interesting global characteristic of the flow is clearly the wave drag D_w exerted by the flow on the obstacle. An ad hoc empirical hydraulic theory proposed by Smith (1985) suggests the scaling $D_w \sim U^3/N$. The normalized values of drag are shown in Fig. 8a (original values of the drag are also shown using a logarithmic scale in Fig. 8b). The estimated values of the wave drag
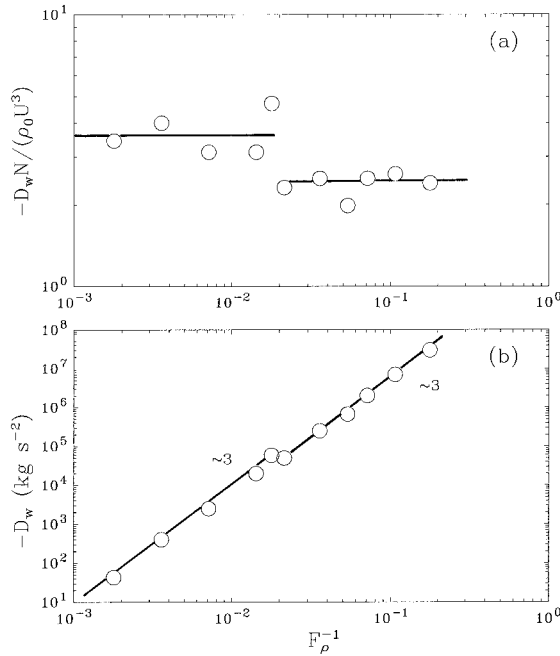
FIG. 8. Drag as a function of the parameter $(F_\rho)^{-1}$: (a) in nondimensional form and (b) in dimensional form in log–log coordinates.

FIG. 9. Characteristics of pulsations of the surface velocity as functions of the parameter $(F_\rho)^{-1}$: (a) nondimensional values of the maximum surface velocity; (b) nondimensional phase velocity; and (c) nondimensional horizontal wavelength. Different symbols denote different ways of determination of the wavelength: ($\bigcirc$) the values obtained from the spatial spectra of the perturbations, and (*) $\lambda = c_{ph}T$, where the period T of pulsations is obtained from the temporal spectra.

are taken when the flow has fully developed in the sense that the drag has reached a level of statistical equilibrium in which it has ceased to grow. Although these values of drag show an unsurprisingly large scatter, it is clearly observed in Fig. 8a that a rather abrupt transition occurs from a larger to a smaller value as the parameter F_ρ^{-1} increases. Thus, with increasing F_ρ^{-1} the power law for the drag remains the same, but the coefficient of proportionality decreases abruptly by about 40%.

The question arises as to why this previously unrecognized and rather dramatic transition occurs. As we will demonstrate, it appears that the answer lies in the dynamics of the Kelvin–Helmholtz (K–H) instability that develops in the shear layer that forms on the interface between the low-level jet and the overlying decelerated region that characterizes the new "mean flow" in the lee of the obstacle that is induced by wave breaking. A comparison of Figs. 6a and 6c suggests that the amplitude of the K–H-related perturbations is significantly more intense for larger U. The numerical data do indeed support this interpretation. For example, the ratio of the amplitude of the pulsations of surface velocity to the inflow velocity increases with F_ρ^{-1} (Fig. 9a), as does the phase velocity of the downstream-propagating pulsations (Fig. 9b), which begins to rise from a constant value of unity for $F_\rho^{-1} \geq 0.02$ (this phase velocity is measured as the mean slope of the streaks of anomalously high velocity in the Hovmöller diagrams). Without providing any detailed demonstration of the fact, we simply note that there is no obvious dependence of the phase velocity on the Reynolds number, while the
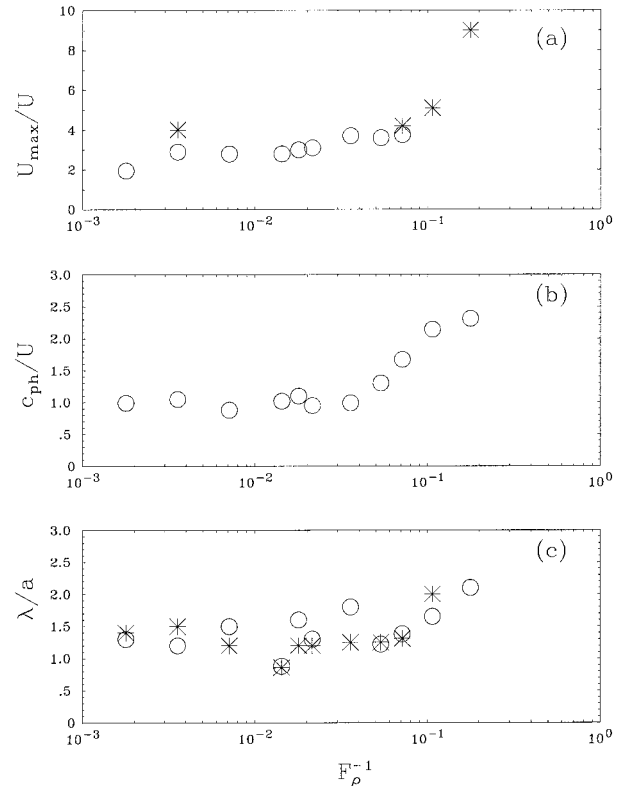
amplitude of pulsations does increase with Re (for given F_ρ^{-1}).

It is well known that a stably stratified parallel flow is potentially unstable if the gradient Richardson number $\mathrm{Ri} = N^2(du/dz)^{-2} < 0.25$ for some z (Miles 1961; Howard 1961). Although the exact critical value of Ri may differ from 0.25 in the present case, in which the basic-state flow is not a one-dimensional parallel flow and has a proximate lower horizontal boundary, we nevertheless expect that instabilities should appear for sufficiently small Ri and that in general their growth rate should increase dramatically as Ri decreases. The Richardson number characteristic of the flow should clearly scale as $\mathrm{Ri} \sim N^2L^2/U^2$. If one chooses a characteristic vertical scale, L, to be proportional to the height of the wave-induced critical level, the minimum Richardson number in a shear layer would be expected to vary as

$$\mathrm{Ri}_{\min} = c_1\left[1 - \left(\frac{2}{3\pi F_\rho}\right)^{1/2}\right], \qquad (33)$$

where the coefficient c_1 may be determined on the basis of numerical experimentation. Previous related numerical calculations (e.g., Peltier et al. 1978), where tem-
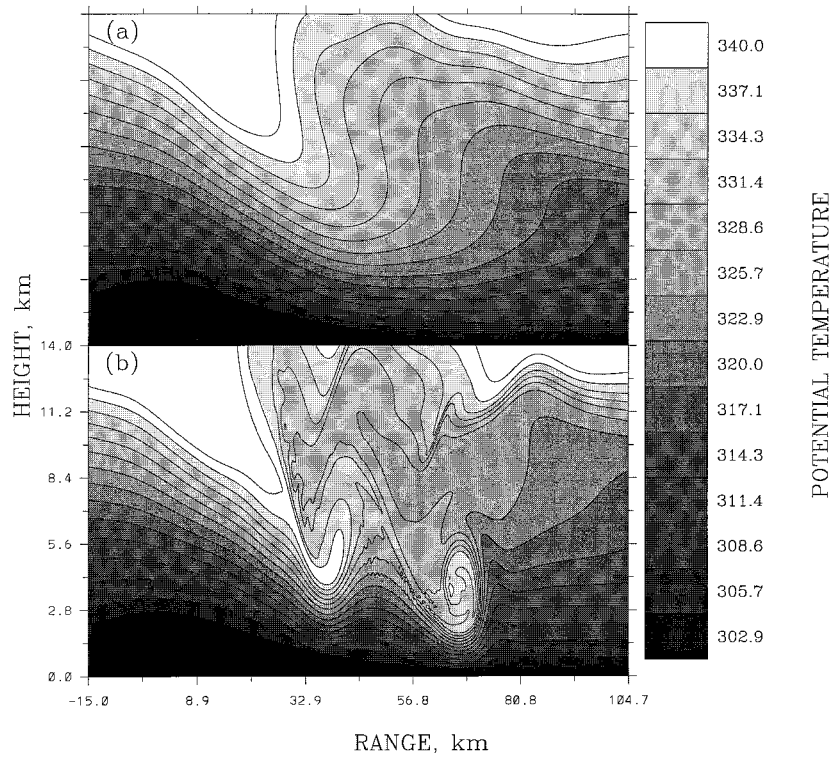
FIG. 10. Contour plots of potential temperature for the simulation with $U = 30$ m s^{-1} (line 15 in Table 1) at (a) $t = 60$, (b) 90 min.
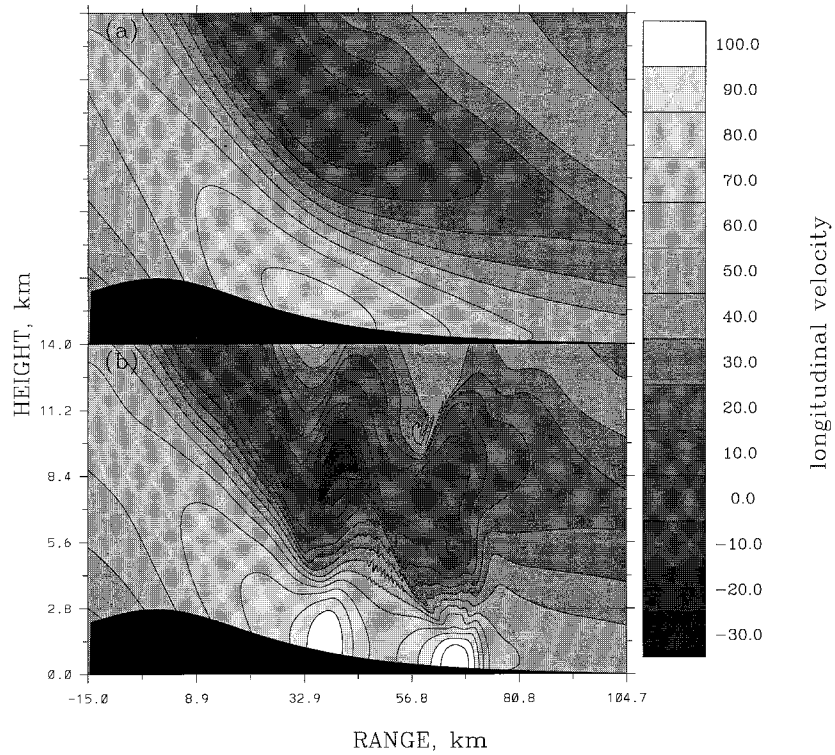
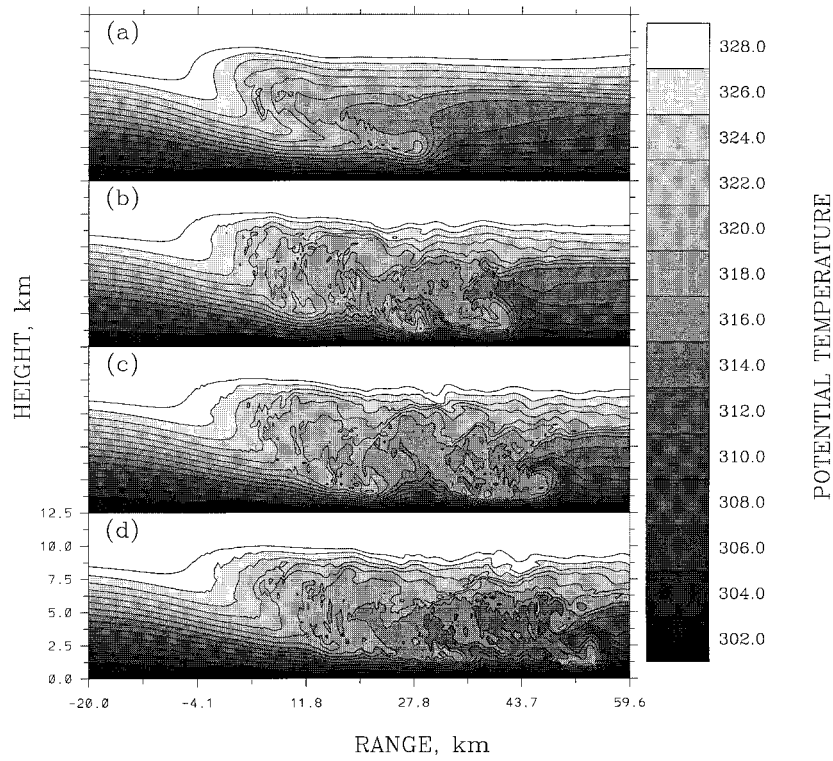

FIG. 11. As in Fig. 10 but plots of horizontal velocity.

FIG. 12. Contour plots of potential temperature for two-dimensional simulations at (a) t = 130, (b) 160, (c) 170, (d) 180 min. The three-dimensional calculations were initialized from the two-dimensional calculations with U = 15 m s^{-1} (line 11 in Table 1) at time t = 120 min. The X–Z sections of the flow at y = 30Δy are shown.
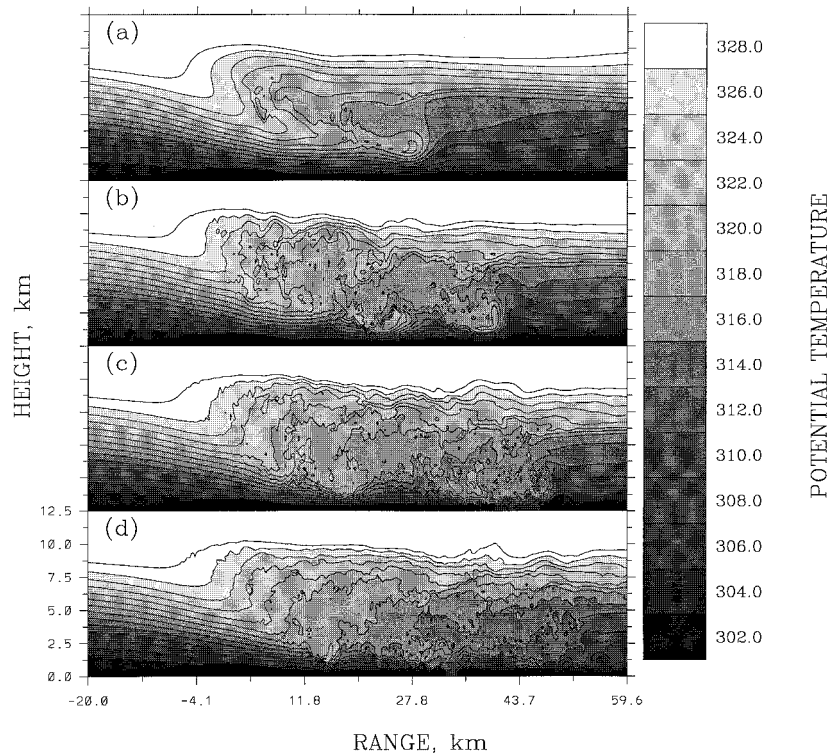
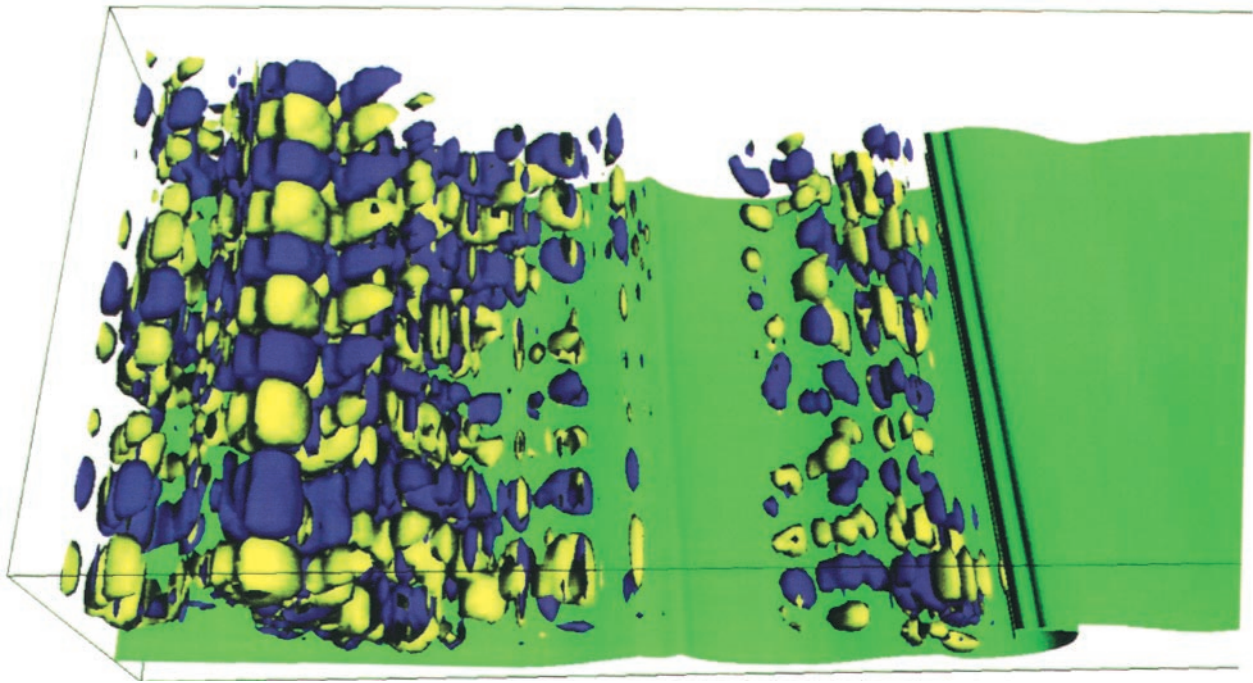FIG. 13. As in Fig. 12 but for three-dimensional simulations.

FIG. 14. Isosurfaces of the streamwise component of vorticity: $\omega_y = \pm 1.4 \ 10^{-3} s^{-1}$, $t = 150$ min. The green surface represents the potential temperature isosurface $\theta = 312$.
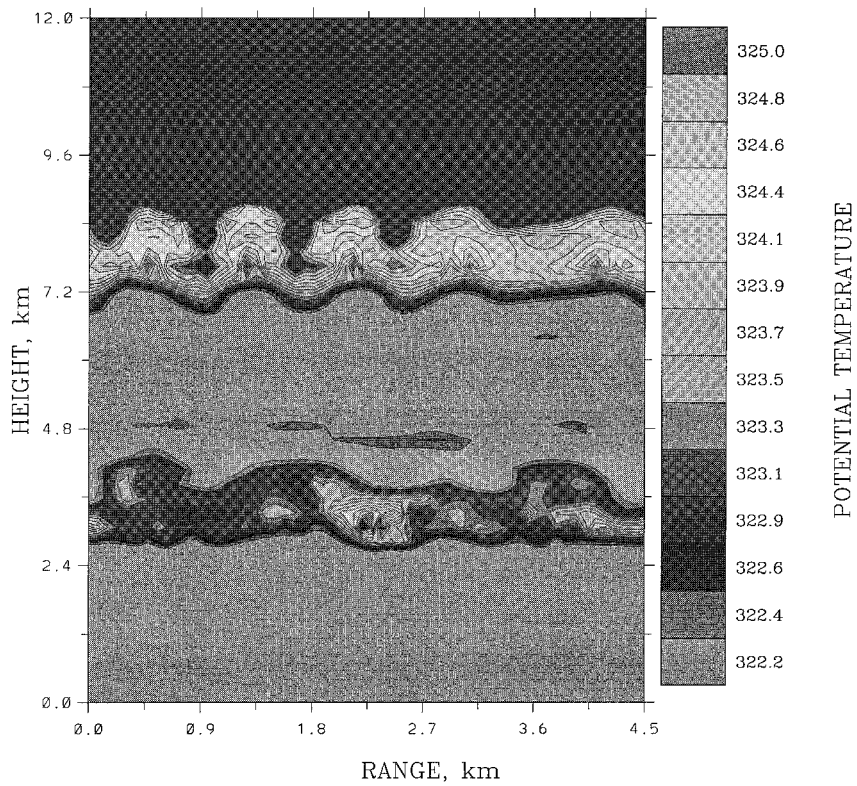

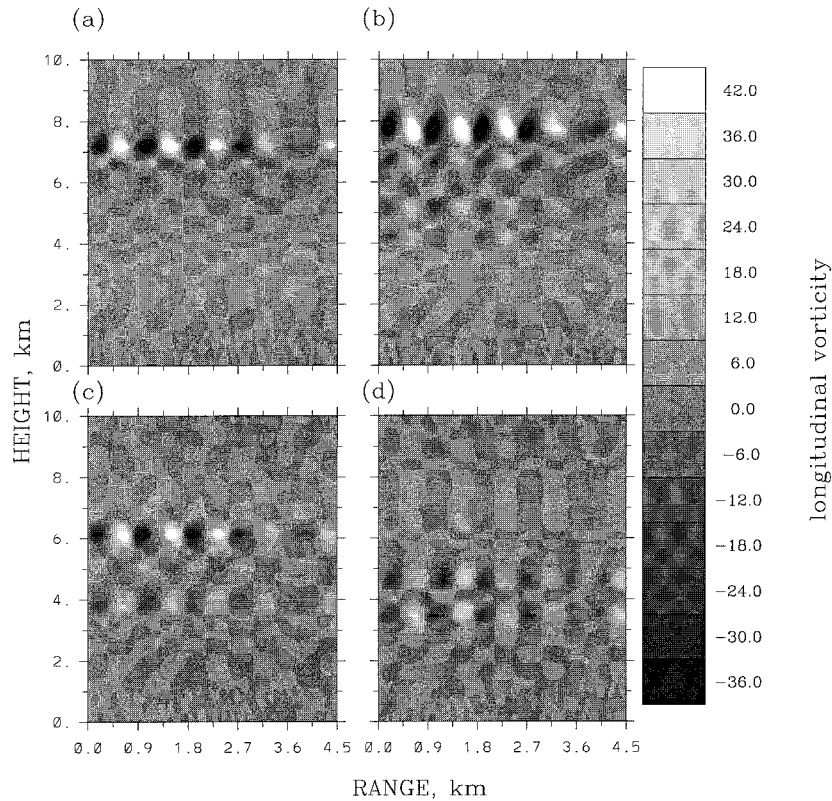FIG. 15. Contour plot of potential temperature in Y–Z plane at $x = 12$ km, $t = 155$ min.

FIG. 16. Contour plots of streamwise component of vorticity (ω_x) at different Y–Z planes.
Region of wave breaking (a) $x = 6$, (b) 7.2, (c) 8.4, (d) 9.6 km.

porally and spatially averaged flows were employed for the determination of Ri for a flow with $U = 5$ m s^{-1} ($F_v = 1$, $F_h = 10$, $F_\rho = 1.8 \times 10^{-2}$, Re $\rightarrow \infty$), give a value for c_1 that is very slightly greater than 0.25. Since Kelvin–Helmholtz instabilities feedback negatively upon the mean flow in the sense that the vertical shear is sharply diminished by the wave–mean flow interaction process (e.g., Peltier et al. 1978; Klaassen and Peltier 1985a), the value of c_1 for undisturbed flow would clearly be less than the value obtained from data taken at a time when the wave is present in the flow. The source of noise out of which the Kelvin–Helmholtz-like perturbations grow is found in the region of intense wave breaking above the obstacle in which the fluctuations are of convective type, a fact that is confirmed by detailed linear stability analysis (Peltier and Scinocca 1990). There is also some indication that the intensity of perturbations is modulated (see Fig. 6) in the time range 100–250 min (that is consistent with the two-way group delay) for different F_ρ. It seems that the excitation of Kelvin–Helmholtz-like perturbations is of subcritical type for $(F_\rho)^{-1} \lesssim 0.04$, while for larger values of $(F_\rho)^{-1}$, in the supercritical regime, the perturbations become dynamically active in the sense that they determine their own temporal scale. It is notable that there is no obvious dependence of the horizontal wavenumber of the unstable fluctuations upon F_ρ (Fig. 9c). The instability be-

comes the dominant characteristic of the flow for sufficiently large $(F_\rho)^{-1}$, in which regime the flow in the lee of the obstacle consists of several very large-amplitude rolls (Figs. 10, 11), which are typical characteristics of a mature Kelvin–Helmholtz instability. Since the perturbations govern the exchange of horizontal momentum between the low-level high velocity flow and the overlying low velocity flow, it is clear that when the perturbations are stronger, the upper layer will accelerate. Thus, the speed of downstream propagation of the region of modified flow would be expected to increase. In contrast, the drag exerted by the flow on the obstacle would be expected to decrease, since the difference of velocities between the upstream and downstream regions also decreases.

The height of the wave-induced critical level in these numerical simulations was also measured as the unperturbed height of the isotherm for the mean value of temperature in the mixed region produced by wave breaking. The results for this parameter are shown in Fig. 3a, together with the estimate (27) obtained on the basis of linear theory. Though all points obtained in the numerical simulations lie below the theoretical curve, it will be observed that the height nevertheless does decrease with $(F_\rho)^{-1}$. The downstream shift of the breaking region for larger $(F_\rho)^{-1}$ is also noted in the experiments (Fig. 3b).
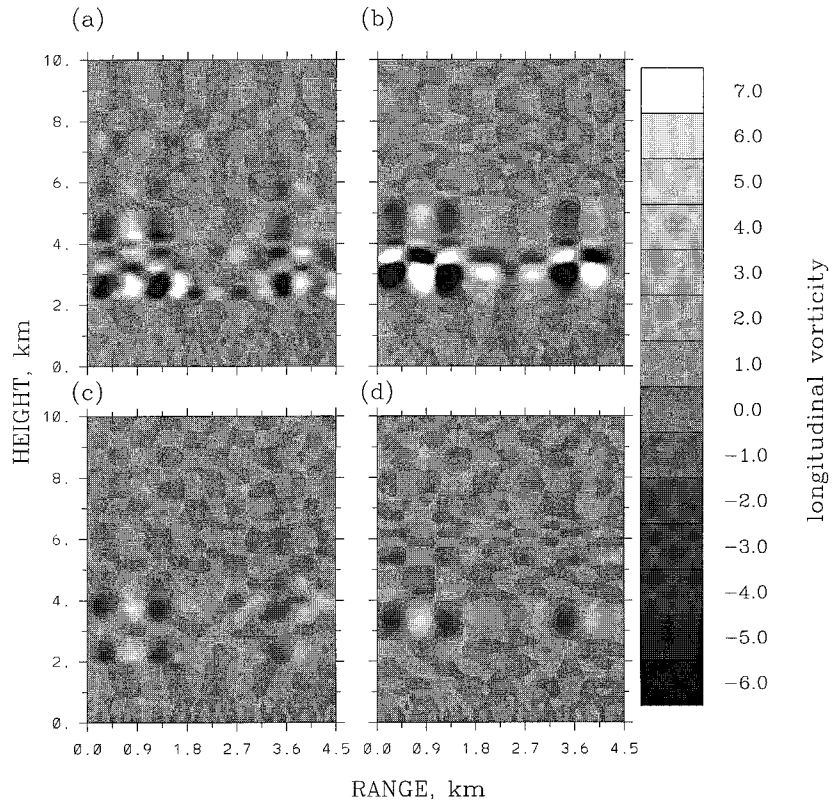
(a)   (b)

(c)   (d)

FIG. 17. As in Fig. 15 but region of K–H roll formation: (a) $x = 12$, (b) 13.2, (c) 14.4, (d) 15.6 km.
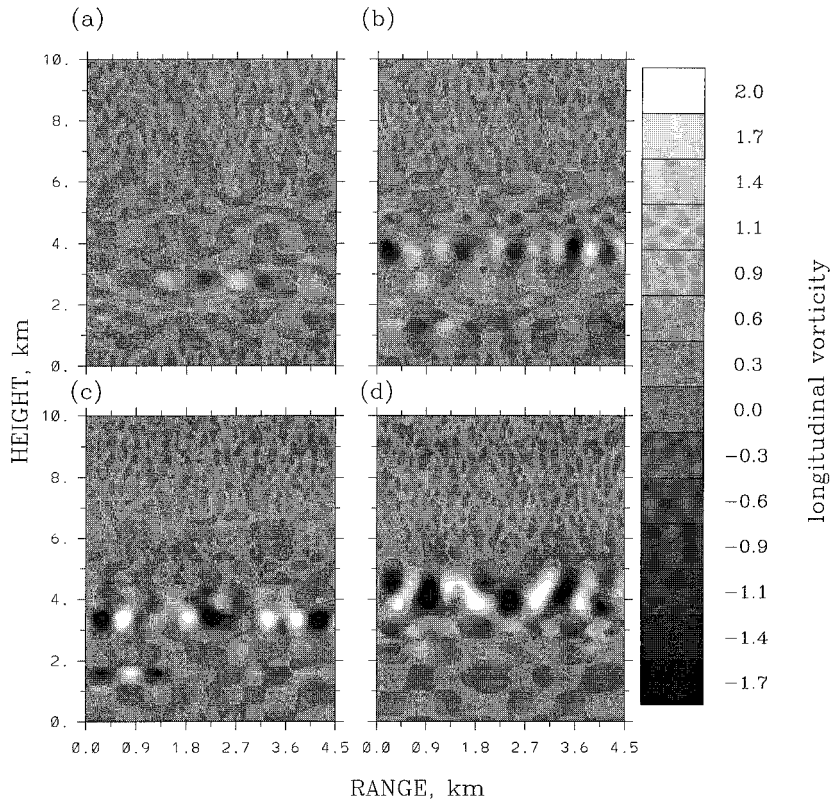
(a)   (b)

(c)   (d)

FIG. 18. As in Fig 15 but region of mature K–H roll: (a) $x = 24$, (b) 26.4, (c) 27.6, (d) 29.6 km.
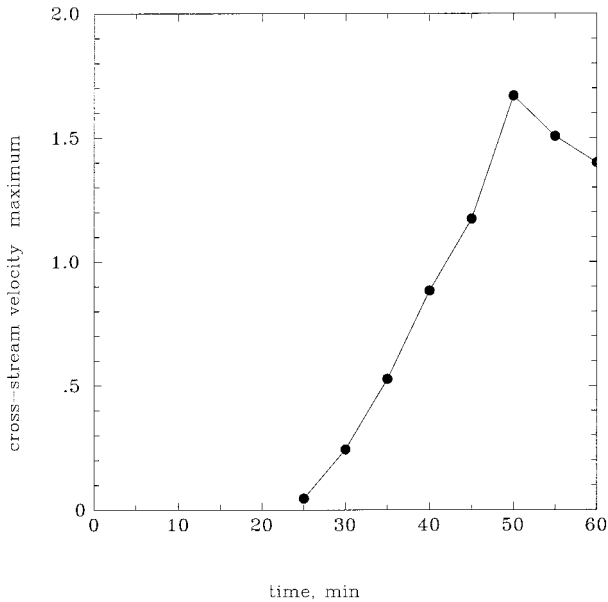
FIG. 19. Temporal behavior of the maximum value of the y component of velocity. The velocity is in nondimensional units (u_y/U).

On the basis of the Hovmöller diagrams it is obvious that the propagation of the chinook front begins after some considerable time following the initialization of a simulation. This "virtual origin time" of the onset of the modified flow regime was also measured (Fig. 3c), and the results are in agreement with our estimate based upon the two-way group delay and therefore consistent with the resonant hypothesis of modified flow formation proposed by Peltier and Clark (1979, 1983), which explains the flow amplification by a resonant interaction of upward- and downward-propagating waves.

6. Three-dimensionalization of the severe downslope windstorm transition

To study the modification of the above-described downslope windstorm states when the flow is allowed to access the third spatial degree of freedom we employ a two-dimensional experiment with $U = 15$ m s^{-1} (line 11, in Table 1) in order to initialize the evolution of the three-dimensional flow. The flow was first allowed to develop in three dimensions only after 60 min of two-dimensional integration, a time by which wave breaking had yet to commence (Figs. 12, 13). A comparison of potential temperature fields in an X–Z section from the three-dimensional flow with the potential temperature
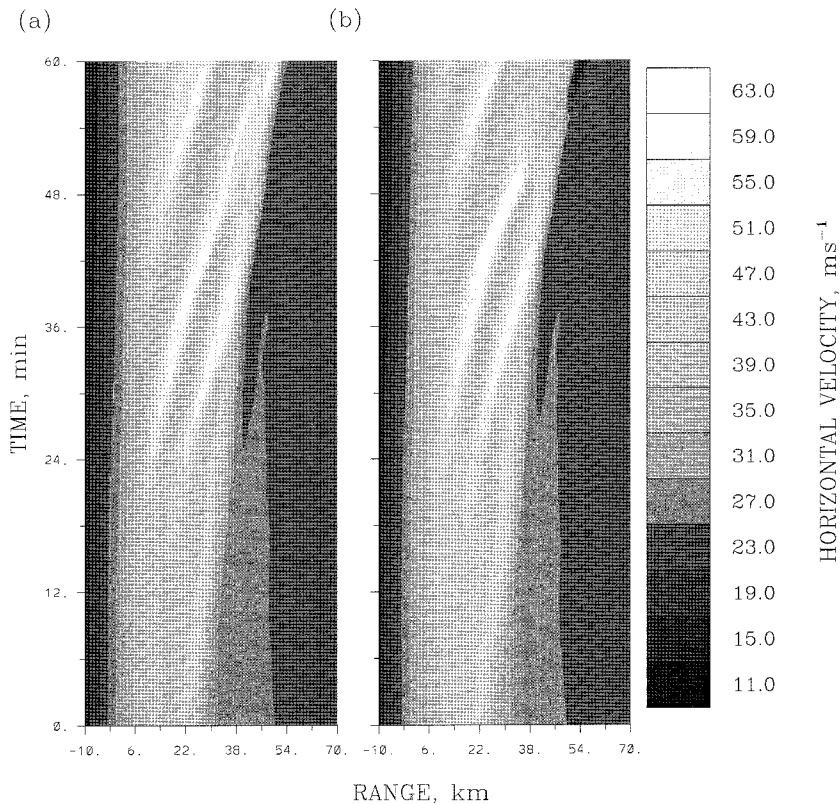

FIG. 20. Hovmöller plots of surface horizontal velocity for (a) two-dimensional and (b) three-dimensional simulations. The x component of velocity averaged in y direction is shown for the three-dimensional case. Time range 120–180 min (0–60 min of three-dimensional calculations).
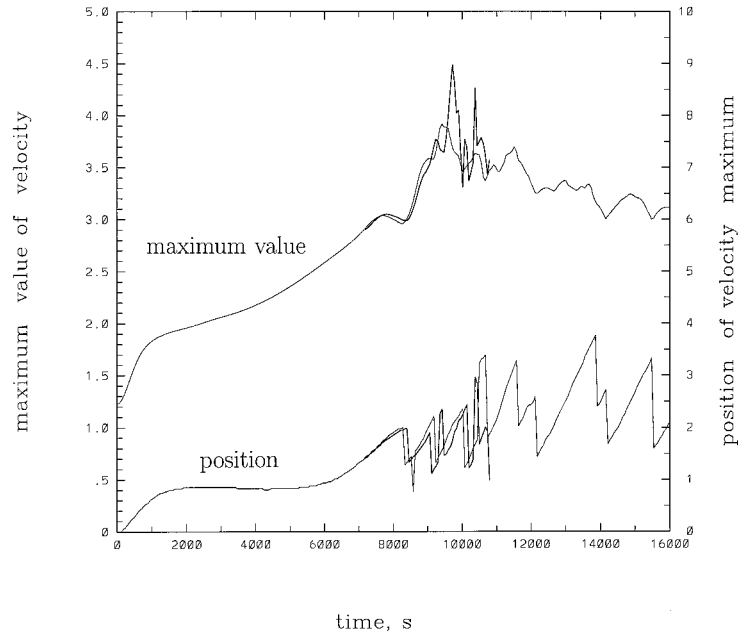
FIG. 21. Temporal behavior of the maximum value of the x component of velocity in nondimensional units, u_x/U (upper curves), and the downstream position of the velocity maximum in nondimensional units, y/a (lower curves). Thin curves represent the two-dimensional simulation, while thick curves represent the three-dimensional simulation for the time range 120–180 min.

field from the two-dimensional flow shows that both fields are essentially identical just subsequent to commencement of three-dimensional integration. Furthermore the y component of velocity and x (streamwise) component of vorticity, both of which are indicators of three-dimensional motions, remain negligible (at the noise level) during the initial 25-min period of three-dimensional integration. These data allow us to conclude that the flow remains stable to three-dimensional perturbations at this stage of its evolution. A second three-dimensional simulation was next initialized after $t = 120$ min of two-dimensional integration, at the time when wave breaking and subsequent formation of K–H billows has just begun (Fig. 13). In this case, three-dimensional motions in the form of streamwise-oriented patches of vorticity of alternating sign develop intensely within the flow (Fig. 14). Diagnostic analyses of data from vertical cross sections (Y–Z planes) of the flow demonstrate that streamwise vortices originate in a region of wave breaking, where the streamlines locally achieve (and excede) a vertical orientation. This region lies between the mountain crest and a distance of approximately one half-width of the mountain downstream.

The results of the present numerical simulations as well as the results of relevant laboratory experiments (Voropayev et al. 1993) concerning the evolution of instabilities in an overturned linearly stratified fluid allow us to propose the following scenario for the development of three-dimensional instability for this case.

The vertically oriented density interfaces become hydrostatically unstable and, as a result, horizontal intrusions appear at different levels, forming horizontal layers. Thus, the system turns out to consist locally of alternating horizontal layers of relatively denser and lighter fluid. These layers in turn become unstable resulting in the formation of arrays of mushroomlike convective structures (thermals) in the cross-stream (y axis) direction. These structures can be clearly seen in Y–Z sections of potential temperature (Fig. 15). Thus, the convective instability creates a streamwise component of vorticity, which, in combination with streamwise velocity, creates streamwise oriented patches of vorticity of alternating sign. Because there are several unstable layers in this region of the flow, the convective elements appear and grow coherently at different horizontal levels creating a multilayered structure of vortices (Figs. 16–18). A similar mechanism for the generation of streamwise vortex streaks involving convective instability also operates in Kelvin–Helmholtz billows where the overturning motion carries heavy fluid above light fluid. Since the fluid is perturbed already in the wave-breaking region, the perturbations continue to grow in a coherent manner on the K–H billows, which themselves originate in the wave-breaking region. Since there are typically five vortex pairs in the spanwise direction within the model domain (Fig. 16), the dominant spanwise wavelength λ_y of the perturbation can be estimated as $\lambda_y \approx 0.9$ km or $\lambda_y N/U \approx 0.6$ in nondimensional units. This, as might be expected, is of the same order as the typical
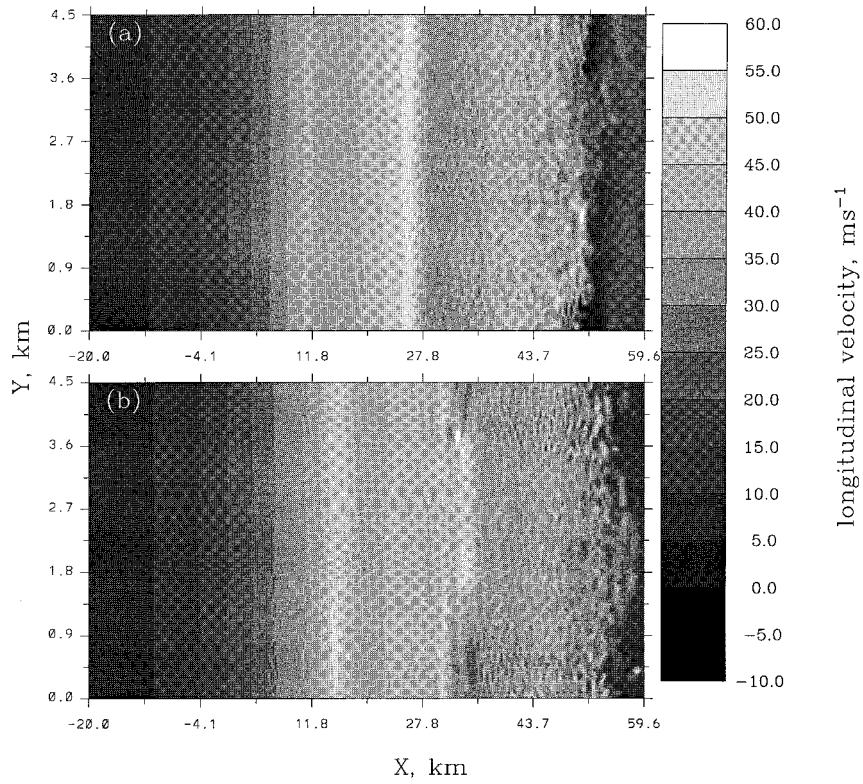
FIG. 22. Contour plots of *x* component of velocity at the surface: (a) *t* = 175, (b) 180 min.
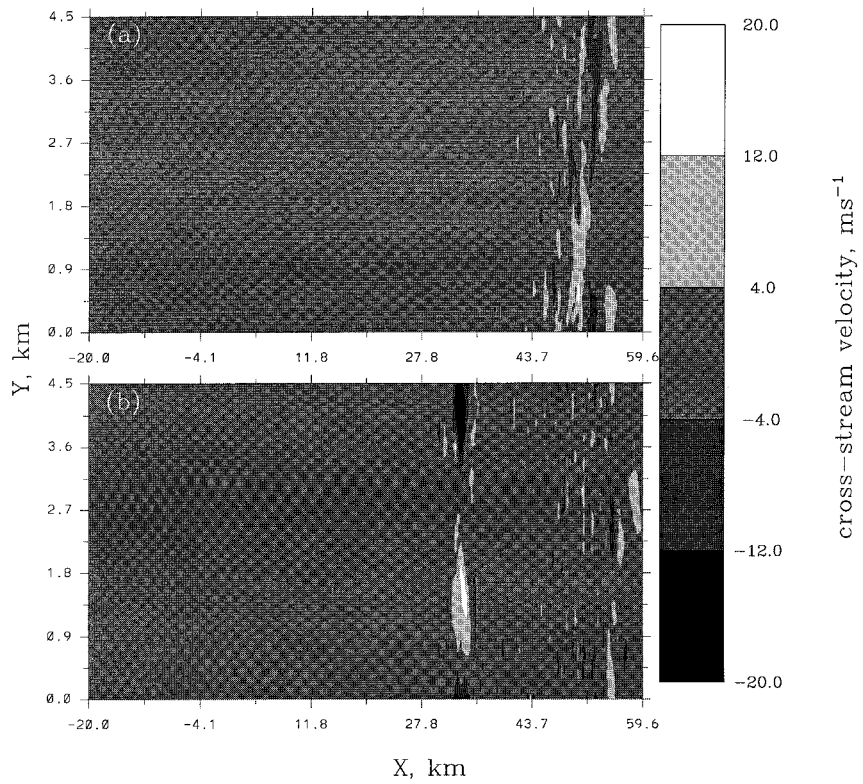

FIG. 23. As in Fig. 22 but for *y* component of velocity.

vertical wavelength of the breaking waves. The ratio of λ_y and the typical wavelength λ_{KH} of K–H perturbations, which in our case is $\lambda_{KH} \approx a$, is then $\lambda_y/\lambda_{KH} \approx 0.06$. This value is consistent with the experimental results by Thorpe (1985) and Schowalter et al. (1994), with prior theoretical predictions of Klaassen and Peltier (1985b) and with the results from high-resolution simulations of breaking Kelvin–Helmholtz waves (Caulfield and Peltier 1994). The streamwise vortices growing on a spanwise billow are transported downstream together with the billow and subsequently erode it through the triggering of three-dimensional turbulent motions.

Comparison of the snapshots of potential temperature in Fig. 12 shows that the K–H billows are almost completely destroyed at some distance downstream in the three-dimensional case, while the billows remain coherent to arbitrary distance downstream in the two-dimensional flow. Figure 19 presents the temporal behavior of the maximum value of the y component of velocity (u_y) in the entire computational domain. On this basis it will be noted that the growth of three-dimensional instability ceases at $t \approx 50$ min when the amplitude of the cross-stream velocity is $u_y/U \approx 1.8$ in nondimensional units. Three-dimensional integration was aborted at $t = 180$ min (60 min of 3D integration) because by that time the scale of the turbulent motions had become comparable to the grid scale and we had thus reached the limit of our ability to further resolve the turbulent cascade. In these simulations of the process of threee-dimensionalization, the streamwise vortices were found to be essentially absent from the so-called braid region between the adjacent billow cores (see Fig. 14). This characteristic of the streamwise vortex streaks clearly provides an additional argument in support of the hypothesis that the vortices are created by the shear-aligned convective instability mechanism of Klaassen and Peltier (1985a), rather than by the alternative mechanism that is responsible for the creation of streamwise vortex streaks in unstable unstratified shear layers (e.g., Metcalfe et al. 1987; Klaassen and Peltier 1991; Smyth and Peltier 1994). It is interesting to note that streamwise vorticity is significantly weaker below the cores of K–H billows than above the cores (e.g., Fig. 18). This may be understood to be a consequence of the stabilizing action of high-velocity parallel low-level jet flow.

It is also interesting to consider how the three-dimensional instability influences the flow fields at the surface. This issue is clearly of great practical interest concerning the impacts that natural flows of this kind might be expected to cause. The comparison of Hovmöller diagrams (Fig. 20) for the horizontal velocity in the case of two-dimensional flow with that for the x component of velocity averaged in y direction from the three-dimensional simulation shows that high-velocity pulsations (white streaks of anomalous velocity in the gray-scale diagrams), which are the surface manifestations of individual K–H rolls, do not propagate in

coherent quasi-two-dimensional form as far downstream in the three-dimensional case as they do in the two-dimensional case. This is clearly a consequence of the erosion of the coherence of the two-dimensional K–H rolls by the three-dimensional instability. However, the amplitude of the pulsations is notably larger in the three-dimensional flow. This may be explained with the help of Bernoulli's constraint. The K–H rolls with their embedded streamwise vortex tubes create an effective upper boundary for the low-level jet flow, so that high surface velocity correlates with "shallow" regions under the tubes. Since there are no longitudinal tubes in the two-dimensional flow, it is not suprising that pulsations are less intense in this case. The results presented in Fig. 21 demonstrate that the amplitude of individual pulsations is about 15% larger in three dimensions than in the two-dimensional flow, while the frequency of the pulsations is basically the same. The lower curve in Fig. 21 shows the way in which the velocity maximum located at a point on the surface under a particular K–H roll moves at some constant speed downstream (that is indicated by a constant slope of the curve in this particular time interval) until a new K–H roll appears on the lee slope of the mountain. The process then repeats, creating the sawtoothlike shape of the curve. Contour plots of the longitudinal velocity (Fig. 22) and the cross-stream velocity (Fig. 17ii) at the surface again show that the Chinook front propagating downstream becomes nonuniform in the cross-stream (y axis) direction as a consequence of the erosion of the K–H rolls by the three-dimensional instability. Furthermore, a high velocity streak representing a K–H roll propagating downstream also becomes highly variable in the cross-stream direction (Fig. 17i), as time increases and localized regions of extremely high cross-stream velocity ($u_y \approx \pm 20$ m s^{-1}, $u_y/U \approx \pm 1.3$) appear (Fig. 23b) as the three-dimensional instability matures. It is also worth noting the existence of regions of negative longitudinal velocity at the leading edge of the high velocity flow (black spots in Fig. 22). Similar flow reversals were observed in the Doppler lidar measurements of a windstorm near Boulder, Colorado (Neiman et al. 1988), and were, correctly now according to us, attributed to the hydraulic jump that marks the leading edge of the chinook front. These regions also become highly nonuniform in the cross-stream direction even when the topography is perfectly two-dimensional.

7. Conclusions

The numerical simulations described herein provide clear evidence that Kelvin–Helmholtz instability plays a fundamental role in the global dynamics of stratified flow over topography in both two and three spatial dimensions. Rather than simply being of importance to the small-scale turbulence that is engendered within such flows, the onset of Kelvin–Helmholtz instability entirely governs the intermittency that is an observed

characteristic of the flow in the lee of the topographic maximum. Our two-dimensional simulations show that properties of this instability are extremely sensitive to variations of the governing parameter NU/g, which measures the importance of non-Boussinesq effects. As this parameter increases, the breaking level descends and a local Richardson number characteristic of the low-level flow decreases below its critical value. This results in a dramatic increase of the intensity of the low-level K–H instability. This, in turn, drives a marked change in flow characteristics: the speed of downstream propagation of the chinook front and the intensity of K–H instability induced pulsations of the surface velocity field increase while the drag exerted by the flow on the obstacle decreases.

Three-dimensional simulations initialized from two-dimensional initial conditions show that such severe downslope windstorm flows become convectively unstable to a higher-order instability during the onset of wave breaking. This higher-order instability originates in the wave-breaking region over the mountain where the otherwise stably stratified fluid becomes overturned and then evolves into the low-level K–H rolls where this evolving instability first appears in the form of streamwise-oriented vortices of alternating sign. The physical mechanism that supports the instability is that first analyzed by Klaassen and Peltier (1989) in the context of their analyses of the onset of turbulence in Kelvin–Helmholtz waves. The maturation of this three-dimensional instability eventually erodes the K–H rolls and thereby arrests their downstream propagation. However, the amplitude of the high velocity pulsations that characterize the surface trace of the K–H rolls is significantly higher in three-dimensional flow compared to the amplitudes that this component of the flow is able to reach in two spatial dimensions. The horizontal velocity field at the surface becomes strongly three-dimensional sufficiently far downstream where regions in which the cross-stream component of velocity comes to be of the same order as the streamwise component. These analyses may also be interpreted to mean that the results of previous two-dimensional simulations remain useful in application to flows over two-dimensional topography within several mountain halfwidths downstream of the mountain crest.

REFERENCES

Andreassen, Ø., C. E. Wasberg, D. C. Fritts, and J. R. Isler, 1994: Gravity wave breaking in two and three dimensions. 1. Model description and comparison of two-dimensional evolutions. *J. Geophys. Res.,* **99** (D4), 8095–8108.

Bacmeister, J. T., and M. R. Schoeberl, 1989: Breakdown of vertically propagating two-dimensional gravity waves forced by orography. *J. Atmos. Sci.,* **46,** 2109–2134.

Batchelor, G. K., 1967: *An Introduction to Fluid Dynamics.* Cambridge University Press, 615 pp.

Caulfield, C. P., and W. R. Peltier, 1994: Three dimensionalization of the stratified mixing layer. *Phys. Fluids,* **6,** 3803–3805.

Clark, T. L., 1977: A small-scale dynamic model using a terrain-following coordinate transformation. *J. Comput. Phys.,* **24,** 186–215.

——, and W. R. Peltier, 1977: On the evolution and stability of finite-amplitude mountain waves. *J. Atmos. Sci.,* **34,** 1715–1730.

——, and R. D. Farley, 1984: Severe downslope windstorm calculations in two and three spatial dimensions using anelastic interactive grid nesting: A possible mechanism for gustiness. *J. Atmos. Sci.,* **41,** 329–350.

——, W. D. Hall, and R. M. Banta, 1994: Two- and three-dimensional simulations of the 9 January 1989 severe Boulder windstorm: Comparison with observations. *J. Atmos. Sci.,* **51,** 2317–2343.

Durran, D. R., 1986: Another look at downslope windstorms. Part I: The development of analogs to supercritical flow in an infinitely deep, continuously stratified fluid. *J. Atmos. Sci.,* **43,** 2527–2543.

Gill, E. A., 1982: *Atmosphere-Ocean Dynamics.* Academic Press, 662 pp.

Howard, L. N., 1961: Note on a paper of John W. Miles. *J. Fluid Mech.,* **10,** 509–512.

Klaassen, G. P., and W. R. Peltier, 1985a: The onset of turbulence in finite-amplitude Kelvin–Helmholtz billows. *J. Fluid Mech.,* **155,** 1–35.

——, and ——, 1985b: The effect of the Prandtl number on the evolution and stability of Kelvin–Helmholtz billows. *Geophys. Astrophys. Fluid Dyn.,* **32,** 23–60.

——, and ——, 1985c: The evolution of finite amplitude Kelvin–Helmholtz billows in two spatial dimensions. *J. Atmos. Sci.,* **42,** 1321–1339.

——, and ——, 1989: The role of transverse secondary instabilities in the evolution of free shear layers. *J. Fluid Mech.,* **202,** 367–402.

——, and ——, 1991: The influence of stratification on secondary instability in free shear layers. *J. Fluid Mech.,* **227,** 71–106.

Laprise, R., and W. R. Peltier, 1989a: The linear stability of nonlinear mountain waves: Implications for the understanding of severe downslope windstorms. *J. Atmos. Sci.,* **46,** 545–564.

——, and ——, 1989b: On the structural characteristics of steady finite-amplitude mountain waves over bell-shaped topography. *J. Atmos. Sci.,* **46,** 586–595.

Long, R. R., 1953: Some aspects of the flow of stratified fluids, a theoretical investigation. *Tellus,* **5,** 42–58.

Metcalfe, R. W., S. A. Orszag, M. E. Brachet, S. Menon, and J. J. Riley, 1987: Secondary instability of a temporally growing mixing layer. *J. Fluid Mech.,* **184,** 207–243.

Miles, J. W., 1961: On the stability of heterogeneous shear flow. *J. Fluid Mech.,* **10,** 496–508.

——, and H. E. Huppert, 1969: Lee waves in a stratified flow. Part 4. Perturbation approximation. *J. Fluid Mech.,* **35,** 497–525.

Neiman, P. J., R. M. Hardesty, M. A. Shapiro, and R. E. Cupp, 1988: Doppler lidar observations of a downslope windstorm. *Mon. Wea. Rev.,* **116,** 2265–2275.

Peltier, W. R., 1993: Reply. *J. Atmos. Sci.,* **50,** 3034–3040.

——, and T. L. Clark, 1979: The evolution and stability of finite-amplitude mountain waves. Part II: Surface drag and severe downslope windstorms. *J. Atmos. Sci.,* **36,** 1498–1529.

——, and ——, 1983: Nonlinear mountain waves in two and three spatial dimensions. *Quart. J. Roy. Meteor. Soc.,* **109,** 527–548.

——, and J. F. Scinocca, 1990: The origin of severe downslope windstorm pulsations. *J. Atmos. Sci.,* **47,** 2853–2870.

——, J. Halle, and T. L. Clark, 1978: The evolution of finite amplitude Kelvin–Helmholtz billows. *Geophys. Astrophys. Fluid Dyn.,* **10,** 53–87.

Rottman, J. W., and R. B. Smith, 1989: A laboratory model of severe downslope winds. *Tellus,* **41A,** 401–415.

Schowalter, D. G., C. W. van Atta, and J. C. Lasheras, 1994: A study of streamwise vortex structure in a stratified shear flow. *J. Fluid Mech.,* **281,** 247–291.

Scinocca, J. F., and W. R. Peltier, 1989: Pulsating downslope windstorms. *J. Atmos. Sci.,* **46,** 2885–2914.

Smith, R. B., 1985: On severe downslope winds. *J. Atmos. Sci.,* **42,** 2957–2603.

Smyth, W. D., and W. R. Peltier, 1994: Three-dimensionalization of barotropic vortices on the f-plane. *J. Fluid Mech.,* **265,** 25–64.

Thorpe, S. A., 1985: Laboratory observations of secondary structures in Kelvin–Helmholtz billows and consequences for ocean mixing. *Geophys. Astrophys. Fluid Dyn.,* **34,** 175–199.

——, 1987: Transitional phenomena and the development of turbulence in stratified fluids: A review. *J. Geophys. Res.,* **92** (C5), 5231–5250.

Voropayev, S. I., Y. D. Afanasyev, and G. J. F. van Heijst, 1993: Experiments on the evolution of gravitational instability of an overturned, initially stably stratified fluid. *Phys. Fluids,* **A5,** 2461–2466.

Winters, K. B., and J. Riley, 1992: Instability of internal waves near a critical level. *Dyn. Atmos. Oceans,* **16,** 249–278.